

Electromagnetic description of image formation in confocal fluorescence microscopy

Taco D. Visser* and Sjoerd H. Wiersma

Department of Electron Microscopy, University of Amsterdam, Plantage Muidersgracht 14, 1018 TV Amsterdam, The Netherlands

Received September 10, 1992; revised manuscript received August 23, 1993; accepted September 2, 1993

Using an electromagnetic approach, we calculate the properties of a confocal fluorescence microscope. It is expected that the results will be more reliable than those obtained by conventional scalar theory, the results of which differ significantly from ours. We calculate the point-spread function and the optical transfer function and study the influence of detector size and fluorescence wavelength on the optical sectioning capability. Our calculations are based on electromagnetic diffraction theory in the Debye approximation. The recently noted asymmetry between the illumination and the detection sensitivity distribution is also taken into account.

Key words: confocal microscopy, diffraction, electromagnetic waves, imaging, fluorescence

1. INTRODUCTION

The confocal laser scanning microscope (CLSM) has several advantages over a conventional microscope, such as its superior resolution and its optical sectioning capability. The latter means that only light originating from a small volume around the focus is imaged, whereas light originating from out-of-focus regions is effectively suppressed. This makes it possible to image thick specimens in three dimensions. The sectioning capability is achieved by use of a small pointlike detector. The smaller this detector, the better the optical sectioning of the object. In practice, however, the detector size is limited by signal-to-noise ratio considerations. This is particularly true in the fluorescence mode.

The literature on the theory of image formation in the confocal fluorescence microscope is linked primarily with the names of Sheppard and Wilson and their co-workers,¹⁻⁶ but we also cite Refs. 7 and 8. The studies reported in Refs. 1-8 are entirely scalar in nature. Valuable as they are in explaining the optical sectioning capabilities and the role of the pinhole size, one cannot use scalar (Fourier) diffraction theory with confidence for the quantitative description of any imaging system with an angular aperture of 120° or more, such as a confocal microscope. It would seem that treating light as an electromagnetic phenomenon that satisfies the Maxwell equations is much more suitable under such circumstances. For instance, one expects the results of image restoration by means of deconvolution to be more reliable when the transfer function is derived from an electromagnetic theory than when it is derived from a scalar approach. It is our aim in the present paper to provide an electromagnetic description of the three-dimensional image-formation process in the confocal fluorescence microscope.

We use the electromagnetic diffraction theory of Wolf⁹ and Richards and Wolf¹⁰ to calculate the intensity near the focus of a confocal system. This theory is based on the vectorial equivalent of the Kirchhoff-Fresnel integral

in the Debye approximation. In a recent paper¹¹ we pointed out that the illumination distribution and the detection sensitivity distribution of a confocal fluorescence microscope are not identical, as is usually assumed. By using scalar Fourier theory we showed that a correct derivation of the detection sensitivity distribution leads to a narrower overall point-spread-function (PSF) of the system and, in accordance with this narrower PSF, a better transmittance at higher spatial frequencies, in comparison with previous scalar theories, which do not take this asymmetry into account. We show that by introducing certain modifications into the theory of Richards and Wolf we can now also describe the intensity distribution of the fluorescence signal near the detector in electromagnetic terms. This means that we now have a fully vectorial framework with which the three-dimensional imaging process in a confocal fluorescence microscope can be described. We derive expressions for the three-dimensional transfer function, the PSF, and the optical section capabilities. With our model the influence of the aperture angles of the different lenses, of magnification factors, of detector size, and of fluorescence wavelengths all can be studied.

There is a crucial distinction between scalar and electromagnetic diffraction theory that needs to be emphasized here. Electromagnetic theory describes fields that satisfy the Maxwell equations; it represents our deepest knowledge of nonquantum fields. Only through this approach can polarization effects be described. Furthermore, electromagnetic diffraction theory and scalar theory still give different results for the focusing of an unpolarized beam. A comparison of the intensity as predicted by a nonparaxial scalar theory [Eq. (12.21d) of Ref. 12] and the electromagnetic approach that we use^{9,10} should convince the reader of this. As we demonstrate, the different predictions of the electromagnetic approach warrant its use to describe confocal imaging.

The organization of this paper is as follows. In Section 2 we describe the confocal setup and the theory of Richards and Wolf, and we list the assumptions underlying our approach. In Section 3 we discuss the electromag-

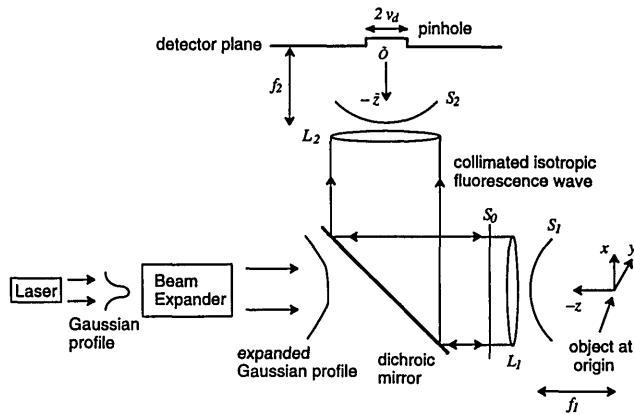


Fig. 1. Model of the confocal fluorescence microscope. An expanded plane laser beam, which is approximately homogeneous, is focused by L_1 onto a fluorescent object that can be scanned mechanically. The focus of L_1 is the origin of the Cartesian coordinates (x, y, z) and the polar coordinates θ and ϕ . L_1 has focal length f_1 and semiaperture angle Ω_1 . The fluorescent light originating from the object is collimated by L_1 and deflected by a dichroic mirror onto L_2 , which in turn focuses the light onto the pinhole detector. L_2 has focal length f_2 and semiaperture angle Ω_2 . The detector, which is placed at the focus of L_2 , has a radius of v_d optical coordinates. The center of the detector coincides with the center of a second set of coordinates $(\bar{x}, \bar{y}, \bar{z})$ and $\bar{\theta}$ and $\bar{\phi}$. The wave fronts S_0 , S_1 , and S_2 are discussed in the text.

netic fields on the wave front that are needed for the diffraction integral, for the cases of both illumination and detection. In Section 4 the intensity in the focal region and near the detector is calculated. In Section 5 the confocal imaging process is analyzed, and a three-dimensional optical transfer function is derived. Several generalizations are discussed, as well. In Section 6 the optical sectioning capabilities of the confocal fluorescence microscope are derived and are compared with results from scalar theory. The microscope's response to both point objects (i.e., the PSF) and planar fluorescent objects is studied for different detector sizes and fluorescence wavelengths. In Section 7 we summarize our results.

2. CONFOCAL MICROSCOPE

A model of the confocal fluorescence microscope is depicted in Fig. 1. The system is symmetric with respect to rotations around the z and the \bar{z} axes. A Gaussian beam with wavelength λ_{ex} produced by the laser is expanded such that an effectively uniform plane wave, S_0 , is incident upon lens L_1 with semiaperture angle Ω_1 . When no aberrations are present, the wave front after refraction coincides with a reference sphere, or rather with that portion of it that approximately fills the exit pupil. The reference sphere, S_1 , has the focal point as its center and has a radius equal to f_1 , the focal length of the lens. The focused light causes an object with a fluorescent material distribution $o(x, y, z)$ to emit fluorescence light. This fluorescence light with wavelength λ_{fl} is collected and collimated by L_1 and is deflected by the dichroic mirror onto the second lens, L_2 (semiaperture angle Ω_2 , focal length f_2), which focuses it onto the detection pinhole. The detector plane coincides with the focal plane of L_2 . The pinhole has a radius (expressed in optical coordinates) of v_d . In practice, the radius of L_2 may be greater than that of L_1 , which means that the aperture of the former will not be

illuminated in its entirety. That means that Ω_2 denotes the semiangle of the emerging light cone rather than the semiaperture of the entire lens. Although we restrict ourselves to an unpolarized incident beam, we need for purposes later in the paper to define the polarization angle α . This is the angle between the amplitude \mathbf{E}_{inc} of the incoming linearly polarized electric field and the positive x axis. The imaging properties of a confocal microscope are strongly determined by the axial intensity distribution. In a system with rotational symmetry, the axial intensity distribution is independent of the state of polarization. In our description we make the basic assumption that the fluorescence response is linear, both in the fluorescent material density and in the excitation intensity. In Section 5 we discuss possible generalizations of our approach.

Before analyzing the complete confocal microscope, we first calculate the electromagnetic field in the focal region of a high-angular-aperture lens with focal length f and semiaperture angle Ω . In Section 4 we specialize our results to lenses L_1 and L_2 . Our starting point is the vectorial theory of Wolf⁹ and Richards and Wolf.¹⁰ This theory expresses the electric-field amplitude $\mathbf{E}(\mathbf{x})$ in the focal region of a high-aperture lens with focal length f in terms of the electric field \mathbf{E}_S in the exit pupil S as

$$\mathbf{E}(\mathbf{x}) = \frac{-ikf}{2\pi} \exp(ikf) \int_{\Gamma} \mathbf{E}_S \exp[-ik(\hat{\mathbf{q}} \cdot \mathbf{x})] d\Gamma, \quad (1)$$

with k the wave number and $\hat{\mathbf{q}}$ a unit vector pointing from the focus in the direction of the point p on the wave front. The integral is over Γ , the solid angle subtended by the aperture at the focal point. Equation (1) is a vector generalization of the Debye integral.¹³ It describes the diffracted field as a superposition of plane waves with amplitudes \mathbf{E}_S whose propagation vectors all lie within the geometrical light cone. For an extensive discussion of the validity of this so-called Debye approximation we refer to the work of Stammes.¹² Here it suffices to say that for a high Fresnel number system, such as a confocal microscope, the approximation is justified. Equation (1) can also be obtained if one starts from the Stratton-Chu integral.¹⁴ The next ingredient that we need is an expression for the electric-field amplitude \mathbf{E}_S on the wave front S for both the illumination and the detection cases. This will be the subject of Section 3.

3. FIELD AMPLITUDES ON THE WAVE FRONT

Let A_{S_i} denote the amplitude of the electric field on wave front S_i , with $(i = 0, 1, 2)$; i.e., $\mathbf{E}_{S_i} = A_{S_i} \hat{\mathbf{E}}_{S_i}$, where $\hat{\mathbf{E}}_{S_i}$ is a unit vector. In order to solve Eq. (1) we first consider how the amplitude A_{S_0} of the incident uniform plane wave front S_0 is connected to the amplitude A_{S_1} of the spherical wave front S_1 after refraction by lens L_1 (see Fig. 1). In the refraction process the energy flux is smeared out. This projection gives \mathbf{E}_{S_1} a θ dependence. Assuming that the lens obeys the sine condition implies that we are dealing with the so-called aplanatic energy projection over the emerging spherical wave front.¹² The sine condition for a plane wave that is incident parallel to the axis reads as

(Ref. 15, p. 168)

$$r = f_1 \sin \theta. \quad (2)$$

This expression means that the rays enter the lens in the object space at the same lateral distance $r = (x^2 + y^2)^{1/2}$ from the z axis as the corresponding ray emerges from the lens in the image space. Furthermore, it implies that a thin annulus with area δS_0 of the incoming plane wave is projected onto a ring-shaped part of the spherical wave with area δS_1 . One can easily show that¹²

$$\delta S_0 = \delta S_1 \cos \theta, \quad 0 \leq \theta \leq \Omega. \quad (3)$$

Conservation of energy then yields for amplitude $A_{S_1}(\theta)$ on spherical wave front S_1

$$|A_{S_1}(\theta)|^2 \delta S_1 = |A_{S_0}(\theta)|^2 \delta S_0. \quad (4)$$

For the uniform excitation beam $A_{S_0} = 1$. So the excitation light traveling to focus under an angle θ with the optical axis has an amplitude

$$A_{S_1}(\theta) = \cos^{1/2} \theta. \quad (5)$$

This apodizationlike effect in high-angular-aperture systems was first discussed by Hopkins.¹⁶

Next consider the fluorescence process. The emitted spherical fluorescence wave has no $\cos \theta$ dependence but is isotropic. When this light, assumed to have unit amplitude, is refracted by L_1 , the reverse of the above geometrical process takes place. So after collimation the light has an amplitude $A_{S_0}(\theta)$, for which

$$A_{S_0}(\theta) = \cos^{-1/2} \theta. \quad (6)$$

Equivalently, one can use the sine condition to express that the isotropic wave originating from focus after collimation by L_1 has an amplitude variation

$$A_{S_0}(r) = \left(1 - \frac{r^2}{f_1^2}\right)^{-1/4}, \quad 0 \leq r \leq f_1 \sin \Omega_1. \quad (7)$$

At refraction by L_2 (notice the change to the second, tilted [see Eq. (8)] system of coordinates centered at its focus), the cosine effect of Eq. (5) again occurs. This means that the emerging converging wave front, which is focused onto the detector, has an amplitude

$$A_{S_2}(\tilde{\theta}) = \left[1 - \left(\frac{f_2}{f_1}\right)^2 \sin^2 \tilde{\theta}\right]^{-1/4} \cos^{1/2} \tilde{\theta}, \quad 0 \leq \tilde{\theta} \leq \Omega_2, \quad (8)$$

where we have again used the sine condition but now for L_2 (see also Ref. 17). Notice that for $f_1 = f_2$ we get $A_{S_2}(\tilde{\theta}) = 1$. We need not worry that the expression between brackets becomes negative. The lateral coordinate r has $f_1 \sin \Omega_1$ as its upper bound. So we have

$$f_2 \sin \tilde{\theta} = f_1 \sin \theta, \quad (9)$$

and hence

$$\left(\frac{f_2}{f_1}\right)^2 \sin^2 \tilde{\theta} = \sin^2 \theta \leq 1, \quad (10)$$

which proves the positivity. It is well known that for an

object in the focal plane of L_1 that is imaged in the focal plane of L_2 , the lateral magnification factor M equals f_2/f_1 . For the angular dependency of the amplitude on the wave front S , substituting this gives

$$A_{S_2;M}(\tilde{\theta}) = (1 - M^2 \sin^2 \tilde{\theta})^{-1/4} \cos^{1/2} \tilde{\theta}, \quad 0 \leq \tilde{\theta} \leq \Omega_2, \quad (11)$$

with the lateral magnification parameter M given by

$$M = \frac{f_2}{f_1} = \frac{\sin \Omega_1}{\sin \Omega_2}. \quad (12)$$

Since A_{S_1} differs from A_{S_2} , we must conclude that the intensity distribution near the focus of L_1 is not equal to the distribution near L_2 . Only in the idealized but physically unrealistic case of a point source and a point detector³ can the PSF of a confocal microscope be written as the square of the excitation intensity. We have shown that when the finiteness of the source is taken into account, that approximation no longer holds.

4. INTENSITY DISTRIBUTION NEAR FOCUS AND THE DETECTOR

Suppose that a uniform linearly polarized beam is focused by a lens. The electric-field amplitude on the converging spherical wave front can be found by use of geometrical reasoning. For details we refer to the paper by Richards and Wolf.¹⁰ An alternative derivation is given by Visser and Wiersma.¹⁸ It turns out that

$$\mathbf{E}_{S;\alpha}(\theta, \phi) = A_S(\theta)(\hat{\mathbf{E}}_1 \cos \alpha + \hat{\mathbf{E}}_2 \sin \alpha), \quad (13)$$

with

$$\hat{\mathbf{E}}_1 = \begin{bmatrix} \sin^2 \phi + \cos \theta \cos^2 \phi \\ \cos \phi \sin \phi (\cos \theta - 1) \\ -\sin \theta \cos \phi \end{bmatrix}, \quad (14)$$

$$\hat{\mathbf{E}}_2 = \begin{bmatrix} \cos \phi \sin \phi (\cos \theta - 1) \\ \cos^2 \phi + \cos \theta \sin^2 \phi \\ -\sin \theta \sin \phi \end{bmatrix}. \quad (15)$$

Here α denotes the polarization angle (the angle between the incident electric field and the positive x axis), and the angles θ and ϕ are defined as usual. The amplitude distribution function $A_{S_i}(\theta)$ is defined in Eq. (5) for the focusing of a uniform beam and in Eq. (11) for the case of a collimated fluorescence beam. Following Richards and Wolf¹⁰ we can now solve Eq. (1) for the first lens, L_1 , with $\mathbf{E}_{S_1;\alpha}$ given by Eq. (13) and $A_{S_1}(\theta)$ by Eq. (5). The integration over ϕ can be carried out by use of an identity for the Bessel functions. This can be done for both polarized and unpolarized light. In the latter case one must also integrate over the polarization angle α . For the axial intensity (which is the main determinant of the optical sectioning properties) the result, of course, will be identical for both cases. For a uniform unpolarized incident beam the outcome for the intensity [or rather the time-averaged electric energy density (Ref. 15, p. 33)] in the focal region is

$$I_{ex}(u, u) = |I_0|^2 + 2|I_1|^2 + |I_2|^2, \quad (16)$$

with

$$I_0(u, u) = \int_0^{\Omega_1} \cos^{1/2} \theta \sin \theta (1 + \cos \theta) J_0 \left(\frac{v \sin \theta}{\sin \Omega_1} \right) \times \exp \left(\frac{i u \cos \theta}{\sin^2 \Omega_1} \right) d\theta, \quad (17)$$

$$I_1(u, u) = \int_0^{\Omega_1} \cos^{1/2} \theta \sin^2 \theta J_1 \left(\frac{v \sin \theta}{\sin \Omega_1} \right) \exp \left(\frac{i u \cos \theta}{\sin^2 \Omega_1} \right) d\theta, \quad (18)$$

$$I_2(u, u) = \int_0^{\Omega_1} \cos^{1/2} \theta \sin \theta (1 - \cos \theta) J_2 \left(\frac{v \sin \theta}{\sin \Omega_1} \right) \times \exp \left(\frac{i u \cos \theta}{\sin^2 \Omega_1} \right) d\theta; \quad (19)$$

here J_n is a Bessel function of the first kind, of order n . [Notice that the angular amplitude distribution function $A_S(\theta)$ is retained in the integrands.] The functions I_n are a function of the dimensionless optical coordinates u and v , which are defined as

$$u = \frac{2\pi}{\lambda_{\text{ex}}} z \sin^2 \Omega_1, \quad v = \frac{2\pi}{\lambda_{\text{ex}}} (x^2 + y^2)^{1/2} \sin \Omega_1, \quad (20)$$

with λ_{ex} the excitation wavelength.¹⁹ We also use the coordinates v_x and v_y , which are defined in a completely analogous manner, but then respectively in the x and the y directions, and for which we have $v = (v_x^2 + v_y^2)^{1/2}$.

Next we turn to the fluorescence process; that is, we study how the second lens, L_2 , focuses a collimated, isotropic fluorescence wave, the properties of which were discussed in Section 3. For the amplitude distribution function $A_S(\theta)$ we must now take Eq. (11). The fluorescence light is assumed to be incoherent and randomly polarized. (Alternatively, one can assume that a fluorescent point object radiates as the sum of an electric and a magnetic dipole.²⁰) Suppose that the detected light has wavelength λ_{fl} . Taking into account the different amplitude distribution function, we now can derive, in the same fashion as Richards and Wolf did for a uniform wave,¹⁰ that for a fluorescence beam the intensity distribution near the detector at the focus of L_2 is, up to a constant, given by

$$\tilde{I}_n(\tilde{u}, \tilde{u}) = |\tilde{I}_0|^2 + 2|\tilde{I}_1|^2 + |\tilde{I}_2|^2, \quad (21)$$

with the functions \tilde{I}_n defined as

$$\tilde{I}_0(\tilde{u}, \tilde{u}) = \int_0^{\Omega_2} A_{S,M}(\tilde{\theta}) \sin \tilde{\theta} (1 + \cos \tilde{\theta}) J_0 \left(\frac{\tilde{v} \sin \tilde{\theta}}{\beta \sin \Omega_1} \right) \times \exp \left(\frac{i \tilde{u} \cos \tilde{\theta}}{\beta \sin^2 \Omega_1} \right) d\tilde{\theta}, \quad (22)$$

$$\tilde{I}_1(\tilde{u}, \tilde{u}) = \int_0^{\Omega_2} A_{S,M}(\tilde{\theta}) \sin^2 \tilde{\theta} J_1 \left(\frac{\tilde{v} \sin \tilde{\theta}}{\beta \sin \Omega_1} \right) \times \exp \left(\frac{i \tilde{u} \cos \tilde{\theta}}{\beta \sin^2 \Omega_1} \right) d\tilde{\theta}, \quad (23)$$

$$\tilde{I}_2(\tilde{u}, \tilde{u}) = \int_0^{\Omega_2} A_{S,M}(\tilde{\theta}) \sin \tilde{\theta} (1 - \cos \tilde{\theta}) J_2 \left(\frac{\tilde{v} \sin \tilde{\theta}}{\beta \sin \Omega_1} \right) \times \exp \left(\frac{i \tilde{u} \cos \tilde{\theta}}{\beta \sin^2 \Omega_1} \right) d\tilde{\theta}. \quad (24)$$

Here we used the abbreviation

$$\beta = \frac{\lambda_{\text{fl}}}{\lambda_{\text{ex}}} \quad (25)$$

to indicate the ratio of the fluorescence and the excitation wavelengths. According to Stokes's law we have $\beta > 1$. $A_{S,M}(\tilde{\theta})$ is given by Eq. (11). Notice that the functions \tilde{I}_n depend on \tilde{u} and \tilde{v} which, just as v and u , are normalized to Ω_1 and λ_{ex} rather than to Ω_2 and λ_{fl} :

$$\tilde{u} = \frac{2\pi}{\lambda_{\text{ex}}} z \sin^2 \Omega_1, \quad \tilde{v} = \frac{2\pi}{\lambda_{\text{ex}}} (\tilde{x}^2 + \tilde{y}^2)^{1/2} \sin \Omega_1. \quad (26)$$

In the remainder of the paper we also use \tilde{v}_x and \tilde{v}_y for describing lateral distances in the x and the y directions.

It should be borne in mind that the effective semiaperture angle Ω_2 of the second lens depends on Ω_1 and the total magnification factor M through Eq. (12), from which

$$\Omega_2 = \sin^{-1} \left(\frac{\sin \Omega_1}{M} \right). \quad (27)$$

5. CONFOCAL IMAGING PROCESS

Suppose that we have a point object emitting fluorescent light with unit intensity, located precisely at the focus of L_1 ; that is, its position vector in optical coordinates, \mathbf{x} , is given by $\mathbf{x} = (0, 0, 0)$. The fluorescent light is collimated by L_1 , and after deflection by the dichroic mirror it is focused onto the detector by L_2 . Hence the intensity in the detector plane, which we call I_d , is now given by Eq. (21); that is,

$$I_d(\tilde{v}_x, \tilde{v}_y; \mathbf{x}) = \tilde{I}_n(\tilde{v}_x, \tilde{v}_y, 0), \quad \mathbf{x} = (0, 0, 0). \quad (28)$$

Next the point object is shifted laterally to position $\mathbf{x} = (v_x, v_y, 0)$, while its emission intensity is kept fixed. The distribution at the detector is then shifted sideways over a distance $(Mv_x, Mv_y, 0)$, where M denotes the lateral linear magnification that is due to the combined action of L_1 and L_2 [see also Eq. (12)]. Hence

$$I_d(\tilde{v}_x, \tilde{v}_y; \mathbf{x}) = \tilde{I}_n(\tilde{v}_x - Mv_x, \tilde{v}_y - Mv_y, 0), \quad \mathbf{x} = (v_x, v_y, 0). \quad (29)$$

For axial displacements the magnification factor is different. According to the lens law, the distance b of the image to a lens and the distance d from the object to the lens are connected by

$$b = \left(\frac{1}{f} - \frac{1}{d} \right)^{-1}. \quad (30)$$

Thus

$$\frac{db}{dd} = - \left(\frac{1}{f} - \frac{1}{d} \right)^{-2} \frac{1}{d^2} = \frac{-b^2}{d^2} = -M^2. \quad (31)$$

So we find that the axial magnification equals, at least within the focal region, minus the square of the lateral magnification. That means that the intensity in the detection plane that is due to a fluorescent point object located at $\mathbf{x} = (v_x, v_y, u)$ is given by

$$I_d(\tilde{v}_x, \tilde{v}_y; v_x, v_y, u) = \tilde{I}_n(\tilde{v}_x - Mv_x, \tilde{v}_y - Mv_y, M^2u). \quad (32)$$

Now that the system's response to an arbitrarily placed fluorescent point object (with unit emission intensity) has been established, we can find the response to an extended object with a fluorescent material distribution given by $o(\mathbf{x} - \mathbf{x}_s)$, where \mathbf{x}_s denotes the scanning position vector in optical coordinates. We assume that the response of the fluorescent object is linear in both the excitation intensity I_{ex} (i.e., we neglect local saturation effects) and the density of the fluorescent material. Integration over the object, with use of Eq. (32), then yields

$$I_d(\tilde{v}_x, \tilde{v}_y; \mathbf{x}_s) = \int_{-\infty}^{\infty} \int_{-\infty}^{\infty} \int_{-\infty}^{\infty} I_{\text{ex}}(\mathbf{x}) o(\mathbf{x} - \mathbf{x}_s) \times \tilde{I}_{\text{fl}}(\tilde{v}_x - Mv_x, \tilde{v}_y - Mv_y, M^2u) dv_x dv_y du, \quad (33)$$

with $\mathbf{x} = (v_x, v_y, u)$ (notice the \mathbf{x}_s dependence of I_d). The totally measured fluorescence signal $F(\mathbf{x}_s)$ is equal to the integral of I_d over the detector's surface:

$$F(\mathbf{x}_s) = \int_{-\infty}^{+\infty} \int_{-\infty}^{+\infty} \int_{-\infty}^{+\infty} \int_{-\infty}^{+\infty} \int_{-\infty}^{+\infty} I_{\text{ex}}(\mathbf{x}) o(\mathbf{x} - \mathbf{x}_s) \times \tilde{I}_{\text{fl}}(\tilde{v}_x - Mv_x, \tilde{v}_y - Mv_y, M^2u) \times D(\tilde{v}_x, \tilde{v}_y) dv_x dv_y du d\tilde{v}_x d\tilde{v}_y. \quad (34)$$

Here $D(\tilde{v}_x, \tilde{v}_y)$ is the detector efficiency function which for a circular detection pinhole equals

$$D(\tilde{v}_x, \tilde{v}_y) = \begin{cases} 1 & \text{if } \tilde{v}_x^2 + \tilde{v}_y^2 \leq v_d^2, \\ 0 & \text{otherwise} \end{cases}, \quad (35)$$

with v_d the detection pinhole radius, expressed in optical coordinates.

The above derivation of the axial magnification factor M^2 is strictly speaking valid only near the focus, whereas the three innermost integrations in Eq. (34) are over the entire \mathbb{R}^3 . However, both I_{ex} and \tilde{I}_{fl} are sharply peaked around their respective origins, and hence the main contribution to the integral will come from the focal region.

Next we deduce an expression for the incoherent optical transfer function (OTF), or modulation transfer function. To that end one can use the Fourier transform $O(m, n, p)$ of the fluorescent material density distribution, with m , n , and p spatial frequencies in the x , y , and z (or v_x, v_y, u) directions, respectively, to write

$$o(\mathbf{x}) = \frac{1}{(2\pi)^{3/2}} \iiint O(m, n, p) \times \exp[2\pi i(mv_x + nv_y + pu)] dm dn dp, \quad (36)$$

where the m , n , and p integrations extend from minus infinity to plus infinity. Substituting Eq. (36) into Eq. (34) and interchanging the order of integration, we can write the fluorescence signal as the transform of the product of $O(m, n, p)$ and the transfer function $C_{\Omega_1, M, \beta}(m, n, p)$:

$$F(\mathbf{x}_s) = \iiint O(m, n, p) C(m, n, p) \times \exp[-2\pi i(mv_{x,s} + nv_{y,s} + pu_s)] dm dn dp, \quad (37)$$

with the incoherent (or modulation) transfer function $C(m, n, p)$ defined as

$$C(m, n, p) = \int_{-\infty}^{\infty} \int_{-\infty}^{\infty} \int_{-\infty}^{\infty} \int_{-\infty}^{\infty} I_{\text{ex}}(\mathbf{x}) \tilde{I}_{\text{fl}}(\tilde{v}_x - Mv_x, \tilde{v}_y - Mv_y, M^2u) \times D(\tilde{v}_x, \tilde{v}_y) \exp[2\pi i(mv_x + nv_y + pu)] dv_x dv_y du d\tilde{v}_x d\tilde{v}_y. \quad (38)$$

From now on we suppress the parameter list (Ω_1, M, β) in $C(m, n, p)$, just as overall factors. Next we interchange the order of integration and first calculate the integral over the detector. To that purpose, define the function $H(v_x, v_y, u; M)$ as

$$H(v_x, v_y, u; M) = \int_{-v_d - Mv_y}^{v_d - Mv_y} \int_{-(v_d^2 - \tilde{v}_y^2)^{1/2} - Mv_x}^{(v_d^2 - \tilde{v}_y^2)^{1/2} - Mv_x} \tilde{I}_{\text{fl}}(\tilde{w}_x, \tilde{w}_y, M^2u) \times d\tilde{w}_x d\tilde{w}_y, \quad (39)$$

where we have used the transformation $\tilde{w}_x = \tilde{v}_x - Mv_x$ and $\tilde{w}_y = \tilde{v}_y - Mv_y$. The integration is over a circle in the \tilde{w}_x, \tilde{w}_y plane with radius v_d and center $(-Mv_x, -Mv_y)$. Because \tilde{I}_{fl} is a circular symmetric function, rotation of the vector (Mv_x, Mv_y) will alter the domain of integration but not the outcome. In other words, H is circular symmetric in its first two arguments, just like I_{ex} . In Appendix A it is shown that the function H can be transformed into a single integral. Use of its symmetry in the expression for the transfer function gives

$$C(m, n, p) = \int_{-\infty}^{\infty} \int_{-\infty}^{\infty} \int_{-\infty}^{\infty} I_{\text{ex}}(v_x, v_y, u) H(v_x, v_y, u; M) \times \exp[2\pi i(mv_x + nv_y + pu)] dv_x dv_y du. \quad (40)$$

Because of the circular symmetry of I_{ex} and H , the transfer function can be written in a partial Hankel form (Ref. 21, p. 252) as

$$C(q, p) = \int_{-\infty}^{\infty} \int_0^{\infty} I_{\text{ex}}(u, u) H(u, u; M) \times \exp(2\pi i p u) v J_0(2\pi v q) dv du, \quad (41)$$

with q and p spatial frequencies in the lateral v and the axial z directions, respectively. From this expression it follows that the slope of the OTF at $q = 0$ is zero:

$$\left. \frac{\partial C(q, p)}{\partial q} \right|_{q=0} = \lim_{q \rightarrow 0} \left[\int_{-\infty}^{\infty} \int_0^{\infty} I_{\text{ex}}(u, u) H(u, u; M) \times \exp(2\pi i p u) v \frac{\partial J_0(2\pi v q)}{\partial q} dv du \right]. \quad (42)$$

Since $\lim_{x \rightarrow 0} J_0'(x) = 0$ one has

$$\frac{\partial C(q = 0, p)}{\partial q} = 0. \quad (43)$$

For a point detector situated at $\tilde{v}_x = \tilde{v}_y = 0$, which is represented as $D(\tilde{v}_x, \tilde{v}_y) = \delta(\tilde{v}_x) \delta(\tilde{v}_y)$, the transfer function takes the simple form

$$C(m, n, p) = \int_{-\infty}^{\infty} \int_{-\infty}^{\infty} \int_{-\infty}^{\infty} I_{\text{ex}}(\mathbf{x}) \tilde{I}_{\text{fl}}(-Mv_x, -Mv_y, M^2u) \times \exp[2\pi i(mv_x + mv_y + pu)] dv_x dv_y du. \quad (44)$$

(The use of a delta function for a D means that the results

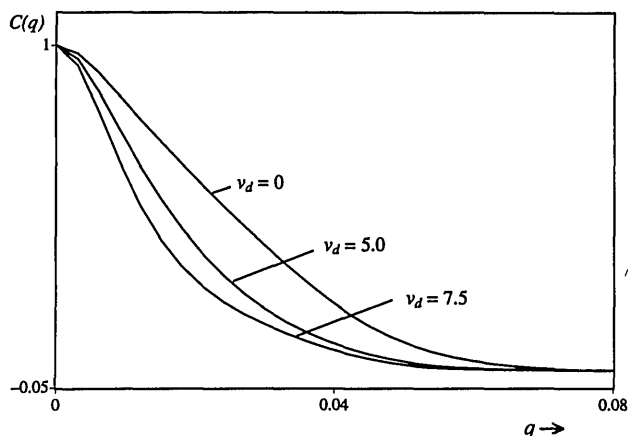


Fig. 2. (Normalized) lateral variation $C(q)$ of the three-dimensional OTF as $p = 0$ for different radii v_d of the detector. $\Omega_1 = 60^\circ$, $M = 10\times$, $\beta = 1.2$. In this and subsequent figures the radii of the pinhole are taken as the size that they have in the confocal region (i.e., true radius divided by M).

for a finite detector converge to the predictions for a point detector as $v_d \rightarrow 0$.) Using the circular symmetry again gives

$$C(q, p) = \int_{-\infty}^{\infty} \int_0^{\infty} I_{\text{ex}}(v, u) \tilde{I}_{\text{fl}}(Mv, M^2u) \times \exp(2\pi i p u) v J_0(2\pi v q) dv du. \quad (45)$$

The incoherent transfer function is a property only of the microscope itself and not of the object. For any spatial-frequency pair (q, p) in the object, the function $C(q, p)$ gives the relative magnitude of the image intensity at those frequencies. Apart from describing the image formation for an arbitrary object, the OTF is also a useful tool for image restoration. (See also the remarks at the end of this section.) For further background on the OTF in confocal microscopy we refer to the paper by Sheppard and Gu.²²

From Eq. (45) it can be seen that the transfer function for a point detector system is the transform of the product of the excitation intensity and the intensity at the detector that is due to a fluorescent point object. Notice that this interpretation is independent of the precise form of the two distributions. We consider next two special cases of Eq. (41). First we consider the function $C(q) \equiv C(q, p = 0)$, which describes the imaging of thick objects with variations only in the lateral direction:

$$C(q) = \int_0^{\infty} v J_0(2\pi v q) \left[\int_0^{\infty} I_{\text{ex}}(v, u) H(v, u; M) du \right] dv. \quad (46)$$

Because of symmetry the integral over u extends over \mathbb{R}^+ only. In Fig. 2, $C(q)$ is shown for several detection pinhole sizes. The transfer function narrows with increasing pinhole radius v_d . Also, the cutoff frequency strongly decreases. For pinhole radii greater than 2.5 the OTF can actually become negative, with the tail of the transfer function oscillating. The negative values of the OTF cause contrast reversals for fine details in the object and hence cause the image fidelity to deteriorate. (Note that the OTF for a single aberration-free lens cannot become negative.) If we compare Eq. (46) with the predictions

of scalar theory,⁴ we see that, although negative values can also occur here, the electromagnetic approach generally predicts a bandwidth that is filled better (for both a point and a finite-sized detector). That is, the half-width of $C(q)$ is a significantly higher percentage of the cutoff frequency than in the scalar case. All this of course has consequences for image restoration by deconvolution.

Second, we consider the function $C(p) \equiv C(q = 0, p)$, the axial variation of the OTF, which is depicted in Fig. 3. $C(p)$ corresponds to the imaging of thick objects with variations only in the axial direction:

$$C(p) = \int_0^{\infty} \int_0^{\infty} I_{\text{ex}}(v, u) H(v, u; M) v \cos[2\pi p u] dv du. \quad (47)$$

Here we see a decrease of the OTF with increasing pinhole size. The deviations from the scalar theory are similar to those of the lateral case. If we normalize p and q to $\sin^2 \Omega_1$ and $\sin \Omega_1$, respectively [see Eqs. (20)], it is found (for the choice of parameters in Figs. 2 and 3) that the resolution in the lateral direction is approximately three times better than the axial resolution.

As an aside, we point out that three generalizations can easily be incorporated into our framework. First, one can assume the incident light to be linearly polarized. This would simply mean that an integration over all polarization angles is left out of the theory (see Ref. 10). The intensity near focus, and hence the response of the system, is then of course no longer axially symmetric.²³ Second, one may want to take aberrations into account by letting the diffraction integral extend over the deformed wave front. This idea is worked out by Visser and Wiersma.¹⁸ Third, the effect of different beam profiles, such as centrally obscured beams and Gaussian beams (or, equivalently, apodized lenses) on the focal electromagnetic-field distribution can be studied by use of the results described in Ref. 14.

Another matter is the influence of the object that is imaged. This influence can take several forms. Scattering and absorption of both the excitation and the fluorescence light may cause the contribution of points deep within the object to become attenuated. An image-processing method has been proposed to compensate for this effect.²⁴

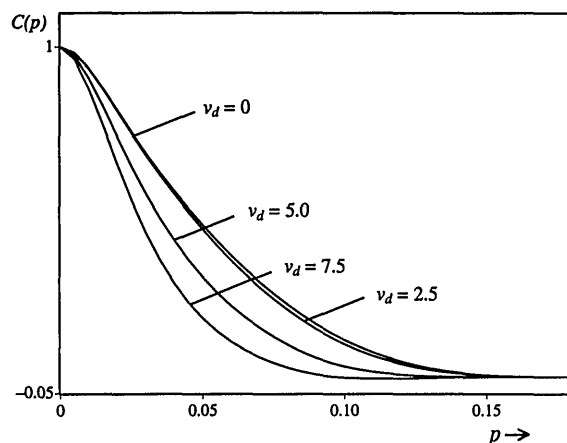


Fig. 3. (Normalized) axial variation $C(p)$ of the three-dimensional OTF as $q = 0$ for different radii v_d of the detector. $\Omega_1 = 60^\circ$, $M = 10\times$, $\beta = 1.2$. The curves for a point detector and $v_d = 2.5$ are very close together on the scale of this figure.

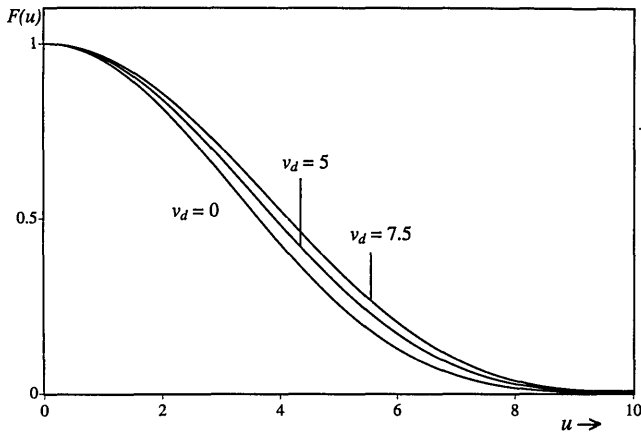


Fig. 4. Detected signal for a point object, axially scanned through focus, for different pinhole radii v_d . The semiaperture angle of the illumination lens L_1 is 60° , the magnification M is $10\times$, and $\beta = \lambda_{fl}/\lambda_{ex} = 1.2$. The response is normalized to $F(0)$.

A refractive-index mismatch between the (oil) immersion fluid and the (watery) object leads to two effects. First, there is a spherical aberrationlike image degradation.²⁵ Second, and even more important, the true distance between the optical sections is then no longer equal to the distance over which the object stage has been moved. If this effect is not taken into account, as is frequently the case, objects may appear to be as much as three times larger than they actually are.²⁶

6. OPTICAL SECTIONING

As noted above, the optical sectioning capability of a confocal fluorescence microscope is achieved by use of a small pinhole in front of the detector. This sectioning property of a CLSM can be described by its response to an object that is axially scanned through the focus. In other words, we want to know how the measured intensity depends on the position of the object that is imaged. Two other parameters that we study below are the pinhole size and the fluorescence wavelength. We therefore return to Eq. (34). For the sake of brevity we omit the scanning position \mathbf{x}_s from now on. Two suitable objects for our purpose are a fluorescent point object and an infinitesimally thin plane with a uniform fluorescence distribution. First, consider the former case: a fluorescent point object placed at $(0, 0, u')$. The object function o is then given by

$$o(\mathbf{x}) = \delta(v_x)\delta(v_y)\delta(u - u'). \quad (48)$$

Using that $I_1(0, u) = I_2(0, u) = \tilde{I}_1(0, \tilde{u}) = \tilde{I}_2(0, \tilde{u}) = 0$ for all u and \tilde{u} and exploiting the rotational symmetry yield

$$F(\tilde{v}; 0, 0, u') = |I_0(0, 0, u')|^2 \int_0^{v_d} \tilde{I}_n(\tilde{v}, M^2 u') \tilde{v} d\tilde{v}. \quad (49)$$

So now we have found the axial PSF for the CLSM. For a point detector at $\tilde{v} = 0$, Eq. (34) reduces to

$$F(0, 0, u') = |I_0(0, 0, u') \tilde{I}_0(0, M^2 u')|^2. \quad (50)$$

Notice that, because the optical coordinate \tilde{v} is dimensionless, F has the same dimension in Eqs. (49) and (50). In Fig. 4 we plot the detected signal F as a function of the axial position u of a fluorescent point object for different

detection pinhole sizes. (The numerical integrations were carried out with routine D01AKF of the NAG library.²⁷) It is clear that a larger pinhole size leads to an increased half-width of the function $F(u)$. In other words, the sectioning decreases when the pinhole becomes larger. On the scale of this figure the curves for a true point detector and one with a radius $v_d = 2.5$ optical units can hardly be distinguished. So one can increase the pinhole diameter to a certain limit in order to improve the signal-to-noise ratio without causing the optical sectioning to deteriorate. On the other hand, it also follows from Fig. 4 that for large pinhole sizes the curves for $F(u)$ change less and less with increasing radius until the entire diffraction pattern is picked up by the detector. Any further increment of the detector size will result only in a decrease of the signal-to-noise ratio. Equation (50) can also be used to study the axial resolution of the microscope. Because we are dealing with a linear system, we can find the response to two point objects a distance δu apart on the axis by evaluating $F(u)$ and $F(u + \delta u)$ and adding the results. This is shown in Fig. 5 for several values of δu . When $\delta u = 5.0$ axial optical units (not shown), the width of the response is increased by 42% compared with the curve for a single point, but the curve still has a single peak. In other words, one cannot really resolve the two points. For $\delta u = 7.5$ the dip is 93% of the peak value. When δu is further increased to 10.0, the dip reduces to a mere 52%.

The second object that we study is an infinitely thin plane with a uniform surface distribution of fluorescent material. The plane is perpendicular to the u axis and is located at $u = u'$. We then have

$$o(\mathbf{x}) = \delta(u - u'). \quad (51)$$

Substituting this into Eq. (34) gives

$$F(u') = \int_{-\infty}^{\infty} \int_{-\infty}^{\infty} \int_{-v_d - Mv_y}^{v_d - Mv_y} \int_{-(v_d^2 - \tilde{v}_y^2)^{1/2} - Mv_x}^{(v_d^2 - \tilde{v}_y^2)^{1/2} - Mv_x} I_{ex}(v_x, v_y, u') \times \tilde{I}_{fl}(\tilde{w}_x, \tilde{w}_y, M^2 u') d\tilde{w}_x d\tilde{w}_y dv_x dv_y, \quad (52)$$

where we have used the transformation $\tilde{w}_x = \tilde{v}_x - Mv_x$ and $\tilde{w}_y = \tilde{v}_y - Mv_y$. In this expression we recognize the

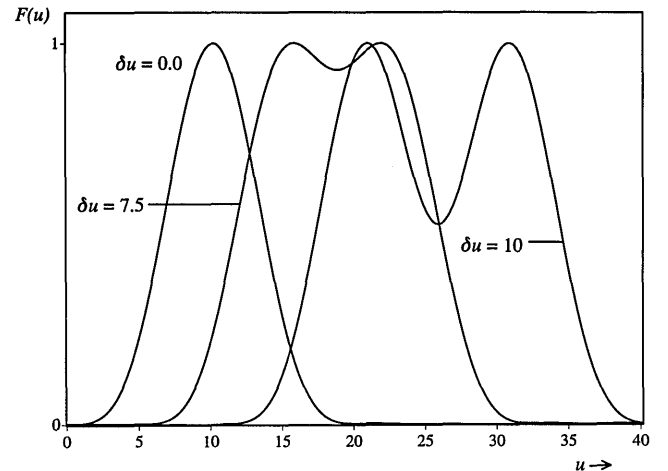


Fig. 5. Response of a confocal fluorescence microscope with a point detector for two point objects on the axis that are a distance δu apart. All curves are normalized to unity. $\Omega_1 = 60^\circ$, $M = 10\times$, $\beta = 1.2$. For clarity the curves have been displaced with respect to one another.

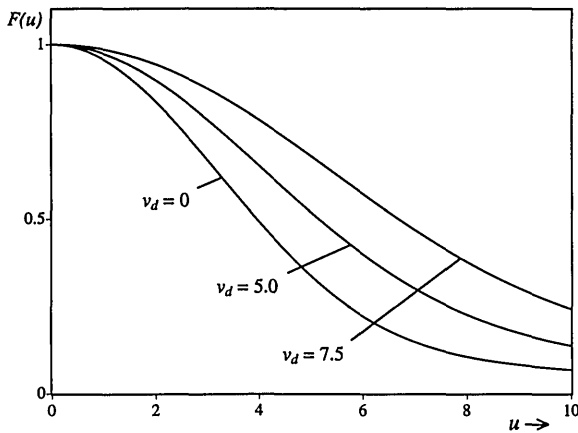


Fig. 6. Detected signal for a perfect planar fluorescent object, axially scanned through the focus of a confocal fluorescence microscope for different values of the detection pinhole radius v_d . $\Omega_1 = 60^\circ$, $M = 10\times$, $\beta = 1.2$.

previously defined function $H(u, u; M)$ of Eq. (39). Substitution yields

$$F(u') = \int_0^\infty I_{\text{ex}}(u, u') H(u, u') v dv. \quad (53)$$

For the case of a point detector at $\tilde{v} = 0$, we have $D(\tilde{v}_x, \tilde{v}_y) = \delta(\tilde{v}_x) \delta(\tilde{v}_y)$, and the expression for $F(u')$ becomes

$$F(u') = \int_0^\infty I_{\text{ex}}(u, u') \tilde{I}_{\text{fl}}(-Mu, M^2 u') v dv. \quad (54)$$

The sectioning of a plane is worse than that of a point object, as follows from a comparison of Fig. 4 with Fig. 6. For instance, the half-width of $F(u)$ when a plane is imaged with $v_d = 5.0$ and $\beta = 1.2$ is approximately 35% greater than when a point is imaged under the same circumstances. The fact that the sectioning of a planar object is worse than that of a point can be understood by consideration of the intensity contours in the u, u plane,²³ from which it can be seen that the intensity I_{ex} (and hence also in approximation the function \tilde{I}_{fl}) for off-axis points within the central peak decreases much less than for a point on the axis when a small excursion in the u direction is made. It should also be noted that for very low aperture angles (i.e., $\Omega \leq 10^\circ$) we retrieve the results from classical paraxial scalar theory.² Also, as can be seen from Fig. 6, the sectioning of a plane is much more sensitive to an increase in the pinhole size than that of a single point. This is because the diffraction pattern at the detector extends over a larger area for a plane than for a point object.

The lateral magnification factor M enters our equations in two ways: first, in the argument of the function I_{fl} [as in Eq. (49)], and second, through the M dependence of the semiaperture angle Ω_2 [see Eq. (27)]. For values of M between 5 and 1000 the curves in Figs. 4 and 6 remain practically identical, as one might expect. For M between 1 and 5 however, deviations up to 15% in the values of $F(u)$ occur. When M gets larger than ~ 1000 , the semiaperture Ω_2 of the second lens L_2 becomes so small that the Debye approximation, and hence our diffraction integral, is no longer valid.²⁸ For such lenses the so-called focal shift phenomenon occurs.²⁹ This means that the intensity pat-

tern at the detector becomes very sensitive to the extent to which lens L_2 is filled (depending of course on the distance L_1-L_2), causing the axial response of the microscope to become asymmetrical. This last point seems clearly an undesired feature of such a design. Incidentally, a vectorial theory that is valid for both high and very low angular aperture focusing has recently been formulated.¹⁴

The next parameter of interest is $\beta = \lambda_{\text{fl}}/\lambda_{\text{ex}}$, the ratio of the excitation and the fluorescence wavelengths. In Fig. 7 the response of a system with a point detector to an axially scanned point object is depicted for several values of β . The limiting value $\beta = 1$ gives the optimal result. From the figure it follows that it is best to keep λ_{fl} as close to λ_{ex} as possible. The dashed curve is the prediction of scalar theory³ for $\beta = 1.0$, which differs significantly from the outcome of our model.

In Fig. 8 the response of a point detector CLSM to an axially scanned fluorescent planar object is shown for different values of β . If we compare these results with the predictions of scalar theory² we find a strong deviation.

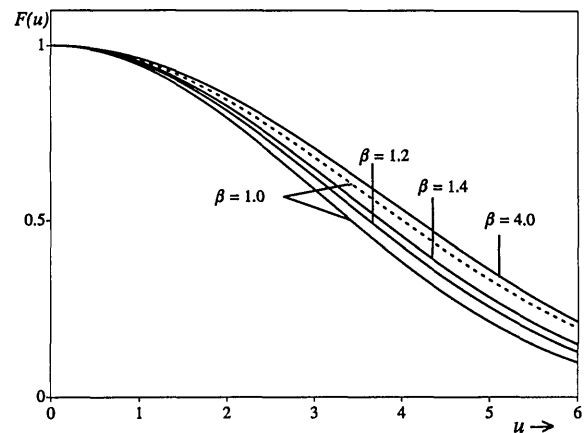


Fig. 7. Response of a confocal fluorescence microscope with a point detector imaging a point object that is axially scanned through focus for different values of $\beta = \lambda_{\text{fl}}/\lambda_{\text{ex}}$. Notice the difference between the predictions of electromagnetic theory (solid curves) and of scalar theory (dashed curve). $\Omega_1 = 60^\circ$ and $M = 10\times$.

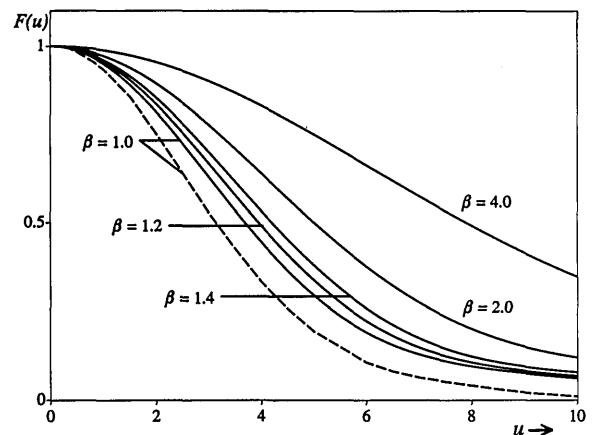


Fig. 8. Detected signal for a perfect planar fluorescent object, axially scanned through the focus of a confocal fluorescence microscope with a point detector for different values of $\beta = \lambda_{\text{fl}}/\lambda_{\text{ex}}$. $\Omega_1 = 60^\circ$ and $M = 10\times$. Dashed curve, the prediction of scalar theory; solid curves, the results according to electromagnetic diffraction theory. Note the large difference between them.

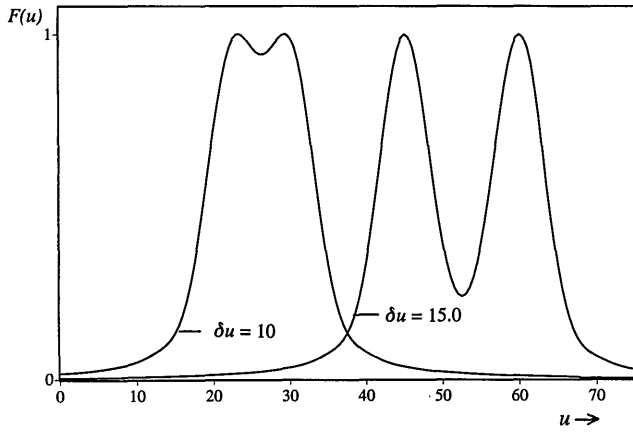


Fig. 9. Response of the confocal fluorescence microscope's imaging of two planes, both of which are perpendicular to the central axis. The distance between the planes is δu optical coordinates. For clarity the curves have been displaced with respect to each other.

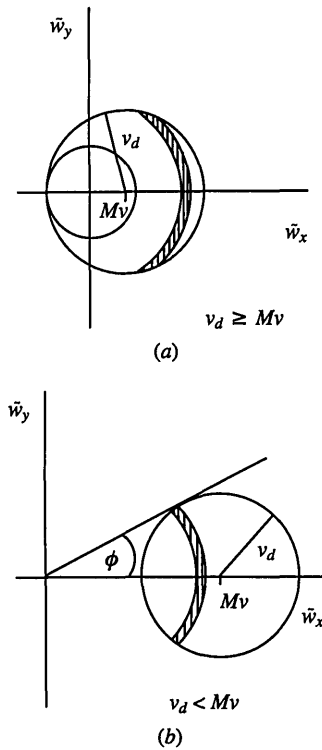


Fig. 10. Region of integration for the function $H(v, u; M)$ for the case in which (a) $v_d \geq Mv$ and (b) $v_d < Mv$.

For $\beta = 1.0$, scalar theory predicts a better sectioning. In addition to the inferior sectioning of a plane compared with that of a point and the greater sensitivity of a plane to the pinhole size, the sectioning of a plane deteriorates much more strongly than the sectioning of a point object when β gets larger.

Finally, the axial two-plane resolution of the confocal microscope is depicted in Fig. 9, where the response to two parallel planes perpendicular to the u axis is shown for two values of δu , their mutual distance. Contrary to the case in Fig. 5, the curve for $\delta u = 7.5$ (not shown) is now still a single peak. For $\delta u = 10.0$ the dip is higher than for the two-point case. This is another way of showing that the

two-plane resolution is worse than the resolution for a two-point object.

7. CONCLUSION

We have presented an electromagnetic theory of the confocal fluorescence microscope. Not only do our results differ significantly from scalar theory, as we have shown with several examples, but we also expect that our approach will give a much more precise description of the imaging process than any scalar theory would. The influence of several factors such as magnification, detection pinhole size, and fluorescence wavelength was studied. It was found in our approach that the modulation transfer function can become negative (even for an aberration-free system) when the detection pinhole size exceeds a certain value. This transfer function can be used for image restoration by deconvolution of confocal images and should give more reliable results than those derived from scalar theory. We calculated the (axial) point-spread function and showed that the optical sectioning of a plane is worse than that of a point object. Also, the former is more sensitive to imaging parameters such as detection pinhole size and fluorescence wavelength. Finally, our analysis showed that when the finiteness of the laser source is taken into account, the overall point-spread function is no longer the square of the excitation intensity.

APPENDIX A: FUNCTION $H(v, u; M)$

In this appendix we evaluate the function $H(v_x, v_y, u; M)$ as a single line integral. From Eq. (39) we have

$$H(v_x, v_y, u; M) = \int_{-v_d - Mv_y}^{v_d - Mv_y} \int_{-(v_d^2 - \tilde{v}_y^2)^{1/2} - Mv_x}^{(v_d^2 - \tilde{v}_y^2)^{1/2} - Mv_x} \tilde{I}_{\Pi}(\tilde{w}_x, \tilde{w}_y, M^2 u) d\tilde{w}_x d\tilde{w}_y. \quad (A1)$$

The integration in the $\tilde{w}_x \tilde{w}_y$ plane is over a circle with center $(-Mv_x, -Mv_y)$ and radius v_d . Because of the circular symmetry, we have $H(v, 0, u; M) = H(v_x, v_y, u; M)$, with $v = (v_x^2 + v_y^2)^{1/2}$. The left-hand side is easier to analyze. First, consider the case in which $v_d \geq Mv$ [Fig. 10(a)]. Using polar coordinates, we transform H into

$$H(v, 0, u; M)_{v_d \geq Mv} = \int_0^{Mv + v_d} \int_{-\Phi(r)}^{\Phi(r)} \tilde{I}_{\Pi}(r) r d\phi dr \quad (A2)$$

$$= \int_0^{Mv + v_d} 2\tilde{I}_{\Pi}(r) r \Phi(r) dr, \quad (A3)$$

with $\Phi(r)$ now to be determined. As can be seen from the figure, the ϕ integration is over the entire 2π as long as $0 \leq r \leq v_d - Mv$. For larger values of r the integration is limited to the hatched circle segment, which is bounded by the intersection of the curves $\tilde{w}_x^2 + \tilde{w}_y^2 = r^2$ and $(\tilde{w}_x - Mv)^2 + \tilde{w}_y^2 = v_d^2$. From the above it follows that

$$\tilde{w}_x = \frac{v_d^2 - r^2 - M^2 v^2}{-2Mv}. \quad (A4)$$

So the point of intersection makes an angle ϕ with the positive \tilde{w}_x axis, for which

$$\phi = \cos^{-1} \left(\frac{v_d^2 - r^2 - M^2 v^2}{-2Mvr} \right). \quad (A5)$$

Summarizing, we have for $v_d \geq Mv$ that

$$\Phi(r)_{v_d \geq Mv} = \begin{cases} \pi & \text{if } 0 \leq r \leq v_d - Mv \\ \cos^{-1}[(v_d^2 - r^2 - M^2v^2)/-2Mvr] & \\ \text{otherwise} & \end{cases} \quad (\text{A6})$$

The other case that we need to consider is that in which $v_d < Mv$. We then have from Fig. 10(b)

$$H(u, 0, u; M)_{v_d < Mv} = \int_{Mv-v_d}^{Mv+v_d} \int_{-\Phi(r)}^{\Phi(r)} \tilde{I}_{\Pi}(r) r d\phi dr \quad (\text{A7})$$

$$= \int_{Mv-v_d}^{Mv+v_d} 2\tilde{I}_{\Pi}(r) r \Phi(r) dr. \quad (\text{A8})$$

In precisely the same manner as above we now get

$$\Phi(r)_{v_d < Mv} = \cos^{-1}\left(\frac{v_d^2 - r^2 - M^2v^2}{-2Mvr}\right). \quad (\text{A9})$$

This concludes the transformation of H into a single line integral.

ACKNOWLEDGMENTS

We thank Koen Visscher for many discussions on the confocal microscope. We also thank H. A. Ferwerda and Colin Sheppard, who suggested several improvements in the original manuscript.

*Present address, Department of Physics and Astronomy, Free University, De Boelelaan 1081, 1081 HV Amsterdam, The Netherlands.

REFERENCES AND NOTES

1. C. J. R. Sheppard and T. Wilson, "Image formation in scanning microscopes with partially coherent source and detector," *Opt. Acta* **25**, 315-325 (1978).
2. T. Wilson, "Optical sectioning in confocal fluorescent microscopes," *J. Microsc.* **154**, 143-156 (1989).
3. T. Wilson and C. J. R. Sheppard, *Theory and Practice of Scanning Optical Microscopy* (Academic, London, 1984).
4. M. Gu and C. J. R. Sheppard, "Confocal fluorescent microscopy with a finite-sized circular detector," *J. Opt. Soc. Am. A* **9**, 151-153 (1992).
5. T. Wilson, "The role of the pinhole in confocal imaging systems," in *Handbook of Biological Confocal Microscopy*, J. B. Pawley, ed. (Plenum, New York, 1990).
6. C. J. R. Sheppard, "Axial resolution of confocal fluorescence microscopy," *J. Microsc.* **154**, 237-241 (1989).
7. S. Kimura and C. Munakata, "Calculation of three-dimensional optical transfer function for a confocal scanning fluorescent microscope," *J. Opt. Soc. Am. A* **6**, 1015-1019 (1989).
8. S. Kawata, R. Arimoto, and O. Nakamura, "Three-dimensional optical-transfer function analysis for a laser-scan fluorescence microscope with an extended detector," *J. Opt. Soc. Am. A* **8**, 171-175 (1991).
9. E. Wolf, "Electromagnetic diffraction in optical systems I," *Proc. R. Soc. London Ser. A* **253**, 349-357 (1959).
10. B. Richards and E. Wolf, "Electromagnetic diffraction in optical systems II," *Proc. R. Soc. London Ser. A* **253**, 358-379 (1959).
11. T. D. Visser, G. J. Brakenhoff, and F. C. A. Groen, "The fluorescence point response in confocal microscopy," *Optik* **87**, 39-40 (1991).
12. J. J. Stamnes, *Waves in Focal Regions* (Hilger, Bristol, UK, 1986).
13. P. J. W. Debye, "Das Verhalten von Lichtwellen in der Nähe eines Brennpunktes oder einer Brennnlinie," *Ann. Phys.* **30**, 755-776 (1909).
14. T. D. Visser and S. H. Wiersma, "Diffraction of converging electromagnetic beams," *J. Opt. Soc. Am. A* **9**, 2034-2047 (1992).
15. M. Born and E. Wolf, *Principles of Optics*, 6th ed. (Pergamon, Oxford, UK, 1980).
16. H. H. Hopkins, "The Airy disc formula for systems of high relative aperture," *Proc. Phys. Soc.* **55**, 116-128 (1943).
17. R. Barakat and D. Lev, "Transfer functions and total illuminance of high numerical aperture systems obeying the sine condition," *J. Opt. Soc. Am. A* **53**, 324-332 (1963).
18. T. D. Visser and S. H. Wiersma, "Spherical aberration and the electromagnetic field in high-aperture systems," *J. Opt. Soc. Am. A* **8**, 1404-1410 (1991).
19. An alternative definition is given by Sheppard and Matthews [J. Opt. Soc. Am. A **4**, 1354-1360 (1987)] that has the advantage that the axial intensity distribution is less sensitive to the aperture angle. Here, however, we follow the definition given by Richards and Wolf.
20. C. J. R. Sheppard and T. Wilson, "The image of a single point in microscopes of large numerical aperture," *Proc. R. Soc. London Ser. A* **379**, 145-158 (1982).
21. R. N. Bracewell, *The Fourier Transform and Its Applications* (McGraw-Hill, New York, 1986).
22. C. J. R. Sheppard and M. Gu, "The significance of 3D transfer functions in confocal scanning microscopy," *J. Microsc.* **165**, 377-390 (1992).
23. A. Boivin and E. Wolf, "Electromagnetic field in the neighborhood of the focus of a coherent beam," *Phys. Rev.* **138**, B1561-B1565 (1965).
24. T. D. Visser, F. C. A. Groen, and G. J. Brakenhoff, "Absorption and scattering correction in fluorescence confocal microscopy," *J. Microsc.* **163**, 189-200 (1991).
25. C. J. R. Sheppard and C. Cogswell, "Effect of aberrating layers and tube length on confocal imaging properties," *Optik* **87**, 34-38 (1991).
26. T. D. Visser, J. L. Oud, and G. J. Brakenhoff, "Refractive index and distance measurements in 3-D microscopy," *Optik* **90**, 17-19 (1992).
27. *Numerical Algorithm Group FORTRAN Library Manual, Mark 14* (NAG Ltd., Oxford, UK, 1991).
28. E. Wolf and Y. Li, "Conditions for the validity of the Debye integral representation of focused fields," *Opt. Commun.* **39**, 205-210 (1981).
29. Y. Li and E. Wolf, "Focal shift in focused truncated Gaussian beams," *Opt. Commun.* **42**, 151-156 (1982).